Draft version May 24, 2016
Preprint typeset using LaTeX style emulateapj v. 5/2/11

arXiv:1605.06655v1 [astro-ph.SR] 21 May 2016

THE SPECTRAL ENERGY DISTRIBUTION OF THE COLDEST KNOWN BROWN DWARF[1]

K. L. Luhman[2,3] and T. L. Esplin[2]

Draft version May 24, 2016

ABSTRACT

WISE J085510.83−071442.5 (hereafter WISE 0855−0714) is the coldest known brown dwarf ($\sim$ 250 K) and the fourth closest known system to the Sun (2.2 pc). It has been previously detected only in the J band and two mid-IR bands. To better measure its spectral energy distribution (SED), we have performed deep imaging of WISE 0855−0714 in six optical and near-IR bands with Gemini Observatory, the Very Large Telescope, and the *Hubble Space Telescope*. Five of the bands show detections, although one detection is marginal (S/N$\sim$3). We also have obtained two epochs of images with the *Spitzer Space Telescope* for use in refining the parallax of the brown dwarf. By combining astrometry from this work and previous studies, we have derived a parallax of $0.449 \pm 0.008''$ (2.23±0.04 pc). We have compared our photometry for WISE 0855−0714 to data for known Y dwarfs and to the predictions of three suites of models by Saumon et al. (2012) and Morley et al. (2012, 2014a) that are defined by the presence or absence of clouds and non-equilibrium chemistry. Our estimates of $Y - J$ and $J - H$ for WISE 0855−0714 are redder than colors of other Y dwarfs, confirming a predicted reversal of near-IR colors to redder values at temperatures below 300–400 K. In color-magnitude diagrams, no single suite of models provides a clearly superior match to the sequence formed by WISE 0855−0714 and other Y dwarfs. Instead, the best fitting model changes from one diagram to the next. Similarly, all of the models have substantial differences from the SED of WISE 0855−0714. As a result, we are currently unable to constrain the presence of clouds or non-equilibrium chemistry in its atmosphere.

Subject headings: brown dwarfs — infrared: stars — solar neighborhood — stars: low-mass — planets and satellites: atmospheres

1. INTRODUCTION

With the discovery of the brown dwarf Gl 229 B (Nakajima et al. 1995; Oppenheimer et al. 1995), it became possible to begin testing atmospheric models within the temperature gap of 100–2000 K between the Jovian planets and low-mass stars (Allard et al. 1996; Marley et al. 1996). Large variations in atmospheric properties (e.g., gas abundances, opacity sources, presence and composition of clouds) are expected across that temperature range (Burrows et al. 2001; Marley & Robinson 2015). As a result, brown dwarfs have been sought at progressively lower temperatures to more fully test models of cool atmospheres. Most of the recent progress in surveys for the coldest brown dwarfs has been enabled by the *Wide-field Infrared Survey Explorer* (*WISE*, Wright et al. 2010), which obtained mid-infrared (IR) images of the entire sky. Those data have been used to greatly expand samples of late-T dwarfs (500–800 K) and to discover members of a new, cooler spectral class, the Y dwarfs (< 500 K, Cushing et al. 2011, 2014; Kirkpatrick et al. 2012, 2013; Tinney et al. 2012; Pinfield et al. 2014; Schneider et al. 2015). A few additional brown dwarfs that are likely members of the Y class have been found as companions through near-IR adaptive optics imaging (Liu et al. 2011, 2012) and mid-IR imaging (Luhman et al. 2011) with the *Spitzer Space Telescope* (Werner et al. 2004). Because the optical and near-IR fluxes of brown dwarfs decrease rapidly with lower temperatures at spectral types later than T6 (<1000 K, Cushing et al. 2011; Kirkpatrick et al. 2011), it is challenging to measure the spectral energy distributions (SEDs) of Y dwarfs for comparison to the predictions of atmospheric models.

The coldest known brown dwarf is WISE J085510.83−071442.5 (hereafter WISE 0855−0714), which has a temperature of $\sim$250 K based on its absolute magnitude at 4.5 μm (Luhman 2014). It has a distance of slightly more than 2 pc, which makes it the fourth closest known system to the Sun. Because of the combination of its close proximity and low temperature, WISE 0855−0714 is a uniquely appealing target for studies of cool atmospheres. In Luhman (2014), the detections of WISE 0855−0714 were limited to broad-band filters at 3–4 and 4–5 μm from *WISE* and *Spitzer*. It was not detected in moderately deep near-IR images ($J = 23$). Additional limits were subsequently placed on its flux in the z', Y, and H bands (Beamin et al. 2014; Kopytova et al. 2014; Wright et al. 2014). Faherty et al. (2014) reported a 2.6 σ detection ($J \sim 25$) in a custom filter within the J band, and they interpreted the resulting color between J and 4.5 μm as evidence of water ice clouds based on a comparison to models of brown dwarfs with and without clouds (Saumon et al. 2012; Morley et al. 2012, 2014a). However, Luhman & Esplin (2014) found that those data were best matched by cloudless models that employed non-equilibrium chemistry.

[1] Based on observations made with the *Spitzer Space Telescope*, the NASA/ESA *Hubble Space Telescope*, Gemini Observatory, and the ESO Telescopes at Paranal Observatory.

[2] Department of Astronomy and Astrophysics, The Pennsylvania State University, University Park, PA 16802, USA; kluhman@astro.psu.edu

[3] Center for Exoplanets and Habitable Worlds, The Pennsylvania State University, University Park, PA 16802, USA

Deeper images of WISE 0855−0714 in multiple bands are needed to better constrain its SED. Because of its exceptional sensitivity, the *Hubble Space Telescope* (*HST*) has been used for much of the near-IR imaging and spectroscopy of Y dwarfs (Cushing et al. 2011, 2014; Kirkpatrick et al. 2012, 2013; Luhman et al. 2014; Schneider et al. 2015). In this paper, we present *HST* observations of WISE 0855−0714 that we have performed in F850LP ($\approx z'$), F105W (wide Y), F110W (wide $Y + J$), and F127M (narrow J). We also have obtained images in the i' band with Gemini Observatory and in a filter encompassing the H-band continuum of brown dwarfs with the Very Large Telescope (VLT). Finally, we have observed WISE 0855−0714 at additional epochs with *Spitzer* to refine its parallax.

2. OBSERVATIONS

In Table 1, we have compiled the telescopes, instruments, filters, exposure times, dates, and program identifications for our imaging of WISE 0855−0714. We have also included all previous *Spitzer* observations of the object (Luhman 2014; Luhman & Esplin 2014; Melso et al. 2015) and two photometric monitoring campaigns with *Spitzer* that will be presented by T. Esplin (in preparation).

2.1. *Selection of Filters*

We have observed WISE 0855−0714 in six optical and near-IR filters to better characterize its SED and in a mid-IR band at 4.5 μm with *Spitzer* to provide additional astrometry for refining its parallax. We also have measured photometry from previous images in a second *Spitzer* band at 3.6 μm. To illustrate how the bandpasses of these filters align with the expected spectral features of WISE 0855−0714, we plot in Figure 1 the filter transmission profiles and an example of a model spectrum for a 250 K brown dwarf at a distance of 2 pc (Morley et al. 2014a). When possible, we selected filters that primarily encompassed continuum emission rather than deep absorption bands, as in the case of F127M on *HST* and the CH_4 continuum filter on VLT. For reference, we include in Figure 1 the $YJHK$ filters from the Mauna Kea Observatories photometric system (Tokunaga et al. 2002).

2.2. *Spitzer IRAC Images*

WISE 0855−0714 has been observed on multiple occasions by *Spitzer*'s Infrared Array Camera (IRAC; Fazio et al. 2004). It contains two 256 × 256 arrays that are currently operating, each with a plate scale of 1.″2 pixel^{-1} and a field of view of 5.′2 × 5.′2. The two arrays cover adjacent areas on the sky in different filters that are centered at 3.6 and 4.5 μm (denoted as [3.6] and [4.5]). Point sources in these bands exhibit FWHM= 1.″7.

All IRAC observations of WISE 0855−0714 are listed in Table 1. Luhman (2014) obtained the data on the first two dates, which were in 2013 and 2014. On the first date, WISE 0855−0714 was imaged in both [3.6] and [4.5]. The primary purpose of the second observation was the measurement of astrometry for WISE 0855−0714, so it was observed only in the band in which it is brightest, namely [4.5]. The next two epochs of data were collected in 2014 by Luhman & Esplin (2014), which were used to measure additional astrometry. The second of those observations consisted of a large map (840″ × 840″) rather than a single field of view of the camera. Melso et al. (2015) performed a second map of the same size in 2015, corresponding to the fifth epoch overall. They searched for companions to WISE 0855−0714 in those two maps based on common proper motions. During all of the observations of WISE 0855−0714 in [4.5], images of a flanking field were taken in [3.6]. As a result, when the two maps were obtained in [4.5], the flanking fields in [3.6] produced maps that encompassed WISE 0855−0714. To continue the astrometric monitoring, we have obtained images in [4.5] on two additional dates in 2015. T. Esplin et al. (in preparation) also have performed continuous imaging of WISE 0855−0714 in [3.6] and [4.5] during two 23 hour periods to characterize its variability.

We have measured astrometry for WISE 0855−0714 from all epochs of [4.5] images except the two photometric monitoring campaigns. During the monitoring for a given filter, WISE 0855−0714 was placed in one corner of the array and held at a fixed location without dithering, which optimizes photometric precision over the course of an observation but produces larger astrometric errors than the standard observing strategy of dithering the target near the center of the array. To measure astrometry for WISE 0855−0714 from the other seven epochs, we applied the methods described in Luhman & Esplin (2014) and the distortion corrections from Esplin & Luhman (2016). The resulting astrometric measurements are presented in Table 2.

We also have measured photometry for WISE 0855−0714 in [3.6] and [4.5] from all of the data except the monitoring campaigns and the second epoch in [3.6]. The latter set of data was excluded because WISE 0855−0714 was slightly blended with a brighter star. WISE 0855−0714 is much brighter in [4.5], so its photometry was unaffected by the neighboring star. For the monitoring campaigns, we have adopted the mean photometry measured by T. Esplin et al. (in preparation). We have measured photometry from the other data with the methods from Luhman et al. (2012). The resulting photometric data are listed in Table 3.

2.3. *VLT HAWK-I Images*

We obtained images of WISE 0855−0714 with the High Acuity Wide-field K-band Imager (HAWK-I) on the Unit Telescope 4 of the VLT. The camera contains four 2048×2048 HAWAII-2RG arrays and has a plate scale of 0.″106 pixel^{-1} (Kissler-Patig et al. 2008). For these observations, we selected a medium-band filter that encompasses the H-band continuum that separates two bands of CH_4 and H_2O absorption (see Fig. 1). Images of WISE 0855−0714 in that filter were taken during portions of six nights across a period of nearly two months (see Table 1). The total exposure time was 6.4 hours. Based on its proper motion and parallax (Section 3.1), WISE 0855−0714 moved $\sim 1''$ between the first and last nights. Therefore, when registering and combining the individual frames from the six nights, we applied offsets to 3″ × 3″ sections of the images surrounding the expected positions of WISE 0855−0714 that compensated for the proper and parallactic motions. Point sources in the final combined image exhibited FWHM$\sim$ 0.″45. We aligned the world coordinate system (WCS) of the image to that of the IRAC images using offsets in right ascension, declination, and rotation that were derived from

sources detected in both sets of data.

A source appears at the expected position of WISE 0855−0714 in the reduced image. A section of the HAWK-I image surrounding that position is shown in Figure 2. The image has been smoothed to a lower resolution of 0.″7 to facilitate visual identification of the detection. We conclude that this source is WISE 0855−0714 since no (stationary) object is detected at that location in the *HST* images, which are deeper than the HAWK-I data. We derived the flux calibration with H-band photometry from the Point Source Catalog of the Two-Micron All-Sky Survey (2MASS, Skrutskie et al. 2006) for sources in the image under the assumption that they have $m_{CH4} - H \sim 0$. Aperture photometry was then measured for WISE 0855−0714 using an aperture radius of 5 pixels and radii of 7 and 11 pixels for the inner and outer boundaries of the sky annulus, respectively. The photometry for WISE 0855−0714 is in Table 3. We have not used the HAWK-I image to measure astrometry for WISE 0855−0714 because the errors would be larger than those from the IRAC and *HST* images, which offer higher a signal-to-noise ratio (S/N) and higher resolution, respectively.

2.4. *HST ACS and WFC3 Images*

At the time of the planning of our initial observations with *HST*, WISE 0855−0714 had been detected only at mid-IR wavelengths. Therefore, we began by observing it in the filter on *HST* that appeared to offer the greatest sensitivity to cold brown dwarfs, F110W on Wide Field Camera 3 (WFC3, Kimble et al. 2008). The same approach was taken by Luhman et al. (2014) in seeking the first near-IR detection of the brown dwarf WD 0806-661 B. After detecting WISE 0855−0714 in F110W, we pursued imaging with *HST* in three additional bands that are aligned with the wavelengths at which much of the near-IR flux is predicted to emerge, consisting of F850LP on the Advanced Camera for Surveys (ACS) and F105W and F127M on WFC3 (see Fig. 1).

We observed WISE 0855−0714 with the IR channel of WFC3 and the Wide Field Channel (WFC) of ACS. WFC3/IR contains a 1024 × 1024 HgCdTe array in which the pixels have dimensions of $\sim 0.''135 \times 0.''121$. ACS/WFC contains two 2048 × 4096 SITe CCD arrays with plate scales of $\sim 0.''05$ pixel^{-1}. For each of the four filters that we selected, WISE 0855−0714 was observed during six orbits that were divided into three two-orbit visits. In a given orbit, one exposure was taken at each position in a three-point dither pattern. The dither patterns in the two orbits in each visit were offset by 3.5 pixels along the x-axis of the array. The position of WISE 0855−0714 predicted by its proper motion and parallax was placed at the IR and WFC1-CTE apertures in WFC3 and ACS, respectively. The WFC1-CTE aperture was selected because it is near one of the readout amplifiers, which minimizes photometric losses due to imperfect charge transfer efficiency. The dates and exposure times for the visits are listed in Table 1.

The WFC3 and ACS images were registered and combined using the tasks *tweakreg* and *astrodrizzle* within the DrizzlePac software package. We adopted drop sizes of 0.85 native pixels and resampled plate scales of $0.''065$ pixel^{-1} and $0.''035$ pixel^{-1} for WFC3 and ACS, respectively. For F110W and F127M, we combined the six exposures within each two-orbit visit, resulting in one reduced images for each of the three visits. WISE 0855−0714 is well-detected in each of those images, as shown in Figures 2 and 3. Because the F127M visits spanned only one week, the movement of WISE 0855−0714 among those visits was very small. As a result, we have included an image from only one of the three F127M visits in Figure 3. Because the S/N of WISE 0855−0714 is low in F850LP and F105W, we combined all exposures from the three visits for each of those filters. As done with the HAWK-I data, we corrected for the expected motion of WISE 0855−0714 among the visits within a small area ($1.''3 \times 1.''3$) surrounding its expected location when registering and combining the images in F850LP and F105W. The reduced images for those filters are shown in Figure 3. WISE 0855−0714 is clearly detected in F105W, but only a marginal detection (S/N∼3) is present in F850LP. Because the F850LP data were taken within a few days of two of the F127M visits, the expected position of the brown dwarf in F850LP is known precisely, and that position does coincide with the weak source indicated in Figure 3.

To measure astrometry for WISE 0855−0714, we began by aligning the WCS of the image from the first F110W visit to that of the HAWK-I image, which was aligned to IRAC (Section 2.3). We then aligned the WCS's of the other WFC3 and ACS images to the new WCS for the first F110W visit. The astrometry for WISE 0855−0714 from each of the visits in F110W and F127M is provided in Table 2. We do not report astrometry from the F850LP and F105W images because of the large errors that result from the low S/N. As with the IRAC astrometry (see Luhman & Esplin 2014), we have estimated the astrometric errors based on the differences in right ascension and declination between different visits for stars with similar magnitudes as WISE 0855−0714.

Aperture photometry was measured for WISE 0855−0714 from each of the reduced images using an aperture radius of four pixels and radii of four and 10 pixels for the inner and outer boundaries of the sky annulus, respectively. For the WFC3 images, we measured aperture corrections of 0.097 (F105W), 0.097 (F110W), and 0.125 mag (F127M) between those apertures and radii of $0.''4$ using bright stars in the images. We then applied those corrections and the zero-point Vega magnitudes of 25.4523 (F105W), 25.8829 (F110W), and 23.4932 (F127M) for $0.''4$ apertures[4] to the photometry of WISE 0855−0714. To calibrate the F850LP photometry, we computed the zero-point STMAG magnitude for a $5.''5$ aperture from the image header keyword *photflam* and converted it the Vega system with the transformation from Sirianni et al. (2005), arriving at a value of 24.316. Because the aperture correction in F850LP is significantly larger for redder objects, we used the software package *synphot* to estimate a correction of 0.68 mag between the aperture applied to WISE 0855−0714 and a $5.''5$ aperture. Drizzled images can contain correlated noise, which would lead to an underestimate of the photometric errors. Therefore, to estimate reliable values for the errors, we created separate versions of the reduced images that used drop sizes of 0.1 native pixels, which should minimize the correlated noise. We then adopted

[4] http://www.stsci.edu/hst/wfc3/phot_zp_lbn

the errors produced by aperture photometry on those images. The photometry in F850LP, F105W, F110W, and F127M is presented in Table 3, where separate measurements are reported for each of the three visits in F110W and F127M.

2.5. *Gemini GMOS Images*

We obtained images of WISE 0855−0714 in the i' filter with Gemini Multi-Object Spectrograph (GMOS) at the Gemini South telescope. We originally proposed to conduct these observations in the z' filter, but we selected i' after deeper imaging in F850LP ($\approx z'$) with *HST* was approved. GMOS contains three 2048×4096 Hamamatsu CCD arrays that have plate scales of $0\farcs08$ pixel^{-1}. WISE 0855−0714 was observed during portions of four nights that spanned nearly two months with a total exposure time of 6.8 hours (see Table 1). The FWHM of point sources in the images ranged from 0.4–0.8″. As done with other data, when registering and combining the individual frames, we compensated for the parallactic and proper motions of WISE 0855−0714 within a 3″ × 3″ section surrounding its expected location. It was not detected in the final combined image (see Figure 3). In Table 3, we provide the magnitude limit in i' that corresponds to S/N=3.

3. ANALYSIS

3.1. *Proper Motion and Parallax*

The proper motion and parallax of WISE 0855−0714 have been previously measured by Luhman (2014), Wright et al. (2014), and Luhman & Esplin (2014). For the most recent measurements, Luhman & Esplin (2014) combined four epochs of astrometry from *Spitzer* with three epochs from *WISE* during its initial survey and after reactivation (*NEOWISE*, Mainzer et al. 2014) that were derived by Wright et al. (2014). Luhman & Esplin (2014) arrived at a proper motion of (μ_α cos δ, μ_δ) =(-8.10 ± 0.02, 0.70 ± 0.02″ yr^{-1}) and a parallax of 0.433±0.015″. We can further refine those parameters with the new astrometry from our IRAC and *HST* images. To do that, we employ the two epochs of astrometry from *WISE* (Wright et al. 2014) after the adjustments by Luhman & Esplin (2014), the astrometry that we have measured from all seven epochs of *Spitzer* [4.5] images in which WISE 0855−0714 was near the center of the array (i.e., excluding the photometric monitoring campaigns), and our astrometry from the six *HST* visits in F127M and F110W. Those data are compiled in Table 2. As mentioned in Sections 2.2 and 2.3, we have not measured astrometry from the F850LP, F105W, and HAWK-I images because the errors would be much larger than those for the other data that we are utilizing. We also exclude the *NEOWISE* astrometry for the same reason. Although the *WISE* data have fairly large errors, we retain them because they significantly extend the baseline of the astrometry.

We performed least-squares fitting of proper and parallactic motion to the 15 epochs of astrometry for WISE 0855−0714 in Table 2 with the IDL program MPFIT. The reduced χ^2 for the resulting fit was 0.4. To verify the errors produced by the fitting, we created 10,000 sets of astrometry that consisted of the sum of the measured astrometry and Gaussian noise. We then fitted parallactic and proper motion to each set. The resulting standard deviations of μ_α, μ_δ, and parallax were similar to the errors from MPFIT. The proper motion and parallax are presented in Table 4. They are consistent with all of the previous estimates. In Figure 4, we plot the relative coordinates among the 15 epochs after subtraction of the best-fit proper motion.

3.2. *Comparison of Observed and Model Photometry*

We wish to compare the available photometry for WISE 0855−0714 to the predictions from models of the atmospheres and interiors of brown dwarfs. A comparison of a given magnitude or color for a brown dwarf to the model predictions can serve as a test of the validity of the model if the defining properties of the brown dwarf are assumed, or it can constrain the properties of the brown dwarf if the model photometry is assumed to be accurate. If several photometric measurements (or a spectrum) are available, then one can pursue both a test of the models and a constraint on the brown dwarf's properties by checking whether one suite of models (e.g., cloudless with equilibrium chemistry) produces a clearly superior fit, and then adopting the properties of the best-fit model from that suite. Such comparisons of data and models can be performed for a single object or for a population. In this section, we summarize previous comparisons of photometry for WISE 0855−0714 to model predictions, compare it and other known Y dwarfs to the models on color-magnitude diagrams (CMDs), and perform a comparison to the full SED that we have measured for WISE 0855−0714.

3.2.1. *Previous Studies of WISE 0855−0714*

Luhman (2014) compared $M_{4.5}$ and a limit on $J-4.5$ for WISE 0855−0714 to the predictions of multiple suites of models and identified the temperature constraint implied by each suite for each of those measurements. A comparison was not performed with $[3.6]-[4.5]$ because theoretical values differ greatly from the observed colors of T and Y dwarfs (Leggett et al. 2010; Beichman et al. 2014). The models considered by Luhman (2014) were defined primarily by the following features: water clouds and chemical equilibrium (Burrows et al. 2003), cloudless and chemical equilibrium (Saumon & Marley 2008; Saumon et al. 2012), cloudless and non-equilibrium chemistry (Saumon & Marley 2008; Saumon et al. 2012), and 50% coverage of water, chloride, and sulfide clouds and chemical equilibrium (Morley et al. 2012, 2014a). In our study, we employ the same models except for those from Burrows et al. (2003), which are omitted because of their poorer agreement with the data for WISE 0855−0714 and other Y dwarfs (Liu et al. 2012; Luhman et al. 2014).

Faherty et al. (2014) obtained images of WISE 0855−0714 in a medium-band filter within the J band, achieving a possible 2.6 σ detection. They used their photometry to estimate the J magnitude of WISE 0855−0714 and place it on a diagram of M_{W2} versus $J-W2$, where $W2$ is a *WISE* band that is similar to [4.5] from *Spitzer*. In that diagram, the brown dwarf appeared closer to the cloudy models from Morley et al. (2012, 2014a) than the cloudless/chemical equilibrium models from Saumon et al. (2012), which they cited as

evidence of water ice clouds. However, using the J estimate from that study, Luhman & Esplin (2014) found that WISE 0855−0714 was roughly midway between the cloudless and cloudy models that assume chemical equilibrium in a diagram of $M_{4.5}$ versus $J - [4.5]$, and that it agreed with cloudless models that invoke non-equilibrium chemistry (Saumon & Marley 2008; Saumon et al. 2012). In general, to draw a definitive conclusion regarding the physical properties of a brown dwarf (e.g., presence of clouds) from a single CMD, one must assume that each suite of models produces colors that are accurate for the physical conditions in question. Such an assumption is not warranted given the untested nature of those colors near the temperature of WISE 0855−0714. Indeed, the suite of models that best matches the data for WISE 0855−0714 and other Y dwarfs varies among different CMDs, as shown in the next section.

Beamin et al. (2014) measured a limit on the Y-band magnitude of WISE 0855−0714. They compared the updated SED to their new version of the BT-Settl models and the cloudy models from Morley et al. (2014a). The best fit models had temperatures of 240 and 250 K, respectively, both with $\log g = 4$. The Y-band limit from Beamin et al. (2014) is similar to the brightest fluxes predicted at the observed value of $M_{4.5}$ for WISE 0855−0714 from among the suites of models that we consider.

Kopytova et al. (2014) obtained z-band images of WISE 0855−0714 that did not show a detection. They compared the SED that included their limit to models of cloudy brown dwarfs from Burrows et al. (2003) and Morley et al. (2014a) for a range of temperatures and surface gravities. During the comparison, each model SED was scaled to match the observed fluxes in [3.6] and [4.5], which was equivalent to scaling the radius. However, that approach can lead to radii that differ significantly from those predicted by evolutionary models for a given temperature and surface gravity (Burrows et al. 2003; Saumon & Marley 2008), and thus are unphysical. Indeed, among the eight best-fit models that they presented, Kopytova et al. (2014) noted that five models exhibited unphysical values of radius (0.4–0.5 $M_{\rm Jup}$) or surface gravity ($\log g > 4.5$). In fact, the gravity and radius of one of their models ($\log g = 5.5$, 1.4 $M_{\rm Jup}$) corresponded to a stellar mass (0.23 $M_\odot$). We find that the best-fit radii of two of their three remaining models also differ from those predicted by evolutionary models by 30–50%. Based on their comparison to the theoretical SEDs, Kopytova et al. (2014) concluded that no models reproduced the [3.6] − [4.5] color of WISE 0855−0714, which was previously known to apply to T and Y dwarfs in general (Leggett et al. 2010; Beichman et al. 2014).

3.2.2. *Color-Magnitude Diagrams*

We can use CMDs to place the photometry of WISE 0855−0714 in the context of data for other brown dwarfs and to compare trends within this population to model predictions. Because few data are available for Y dwarfs in optical bands (Lodieu et al. 2013; Kopytova et al. 2014; Leggett et al. 2015), we have not constructed CMDs with i' and F850LP ($\approx z'$). Previous data for F105W, F110W, F127M, and the CH_4 continuum filter are also limited, but most known Y dwarfs have been observed in the overlapping bands of Y, J, and H (see Fig. 1). Therefore, we select the latter three bands and the two *Spitzer* filters for our CMDs. We plot $M_{4.5}$ on the vertical axis of each diagram because it encompasses less absorption and exhibits higher S/N for Y dwarfs than the other filters, and because it captures most of the flux of Y dwarfs at < 5 μm.

In Figure 5, we show CMDs with colors that extend from $Y/J/H/[3.6]$ to [4.5]. We also plot CMDs with $Y - J$ and $J - H$ in Figure 6. To place WISE 0855−0714 in these CMDs, we have combined our measurements of m_{105}, m_{127}, and m_{CH4} with $Y - m_{105}$, $J - m_{127}$, and $H - m_{CH4}$ as predicted by the models at the value of $M_{4.5}$ for WISE 0855−0714. The three suites of models that we consider (Section 3.2.1) produce similar values of $J - m_{127}$ (∼0.89) and $H - m_{CH4}$ (∼0.85), but the predicted $Y - m_{105}$ ranges from −0.25 to −0.9. We adopted $Y - m_{105} = -0.6$ for plotting WISE 0855−0714 in Figure 5. Its position relative to the models in the $Y - [4.5]$ CMD does not change significantly if a different value is adopted given that the model suites span more than 3 mag in $Y - [4.5]$ at the magnitude of WISE 0855−0714. For m_{127} and [4.5], we have adopted the means of the multiple measurements that are available. WISE 0855−0714 is plotted with an error bar in $J - [4.5]$ that corresponds to the range of the three m_{127} measurements. For [3.6] − [4.5], we have adopted the mean color that was measured in the four epochs with [3.6] data. Because model colors have been used to convert from $m_{105}/m_{127}/m_{CH4}$ to $Y/J/H$ for WISE 0855−0714, the CMDs are technically showing the positions of WISE 0855−0714 relative to the models in $m_{105}/m_{127}/m_{CH4} - [4.5]$ and the positions of other Y dwarfs relative to the models in $Y/J/H - [4.5]$.

In the CMDs, we have plotted a sample of T dwarfs (Dupuy & Liu 2012, references therein) and all known Y dwarfs that have measurements of parallaxes and photometry in relevant bands (Cushing et al. 2011, 2014; Tinney et al. 2012, 2014; Luhman et al. 2012, 2014; Beichman et al. 2013, 2014; Kirkpatrick et al. 2012, 2013; Dupuy & Kraus 2013; Leggett et al. 2013, 2015, 2016; Schneider et al. 2015). For the Y dwarf WISE J035000.32−565830.2 (hereafter WISE 0350−5658), the parallax of $0.291 \pm 0.50''$ from Marsh et al. (2013) places it at a discrepant location in CMDs relative to other Y dwarfs (Leggett et al. 2015, 2016). Meanwhile, four known Y dwarfs lack previous parallax measurements, consisting of WISE J030449.03-270508.3 (Pinfield et al. 2014), WISE J082507.35+280548.5 (hereafter WISE 0825+2805), WISE J120604.38+840110.6 (hereafter WISE 1206+8401), and WISE J235402.77+024015.0 (Schneider et al. 2015). A significant amount of multi-epoch *Spitzer* data is now publicly available for WISE 0350−5658, WISE 0825+2805, and WISE 1206+8401. To resolve the discrepancy in the CMD locations of WISE 0350−5658 and to allow the addition of WISE 0825+2805 and WISE 1206+8401 to the CMDs, we have measured their parallaxes from the *Spitzer* data with the same methods that were applied to WISE 0855−0714, arriving at 0.184 ± 0.01, 0.158 ± 0.007, and $0.085 \pm 0.007''$, respectively. It is likely that these values will be soon superseded by measurements that include the *Spitzer* images that are not yet publicly available as well as astrometry from other telescopes. Using our new parallaxes, all three of these objects exhibit locations in the CMDs that are

consistent with the sequences formed by other Y dwarfs.

For comparison to the data in the CMDs, we have included magnitudes and colors predicted by three suites of models that were mentioned in Section 3.2.1: cloudless with chemical equilibrium, cloudless with non-equilibrium chemistry, and 50% cloud coverage with chemical equilibrium (Saumon & Marley 2008; Saumon et al. 2012; Morley et al. 2012, 2014a). The ages of the Y dwarfs in the CMDs are unknown with the exception of WD 0806-661 B (2±0.5 Gyr, Luhman et al. 2012), so we show model isochrones for ages of 1, 3, and 10 Gyr, which span the ages of most stars in the solar neighborhood. The models with equilibrium and non-equilibrium chemistry are plotted for temperatures of < 450 K and < 350 K, respectively.

In Figure 5, the sequences formed by known Y dwarfs are qualitatively similar among the CMDs with $Y-[4.5]$, $J-[4.5]$, and $H-[4.5]$. The CMD with $[3.6]-[4.5]$ contains the most well-defined sequence because [3.6] and [4.5] usually offer the most accurate photometry for Y dwarfs from available bands. Because of their large scatter, the sequences of Y dwarfs brighter than WISE 0855−0714 in $Y/J/H-[4.5]$ do not tightly constrain the models, but those sequences are in rough agreement with all three model suites, agreeing somewhat better with the cloudless/chemical equilibrium models in $Y-[4.5]$ and $J-[4.5]$. All of the models are much redder than the data in $[3.6]-[4.5]$, as found in a number of previous studies (Leggett et al. 2010; Beichman et al. 2014; Luhman et al. 2014). It is unfortunate that the CMD with the best-defined Y dwarf sequence contains a color that is especially difficult for the models to reproduce. The differences between the three suites of models in the CMDs of $Y/J/H-[4.5]$ increase at fainter magnitudes, so WISE 0855−0714 offers the greatest potential for discriminating among those models. However, the suite of models that best matches the position of WISE 0855−0714 changes from one CMD to the next: cloudless/chemical equilibrium in $Y-[4.5]$, cloudless/non-equilibrium chemistry in $J-[4.5]$, and cloudy in $H-[4.5]$. For the $J-[4.5]$ CMD, Luhman & Esplin (2014) arrived at a similar result using the J-band measurement from Faherty et al. (2014). We note that the overall agreement between the Y dwarf sequences and the model isochrones is not improved by replacing [4.5] with a different band on the vertical axes in the CMDs.

The $Y-J$ CMD in Figure 6 exhibits a well-defined sequence of Y dwarfs plus two blue outliers, WISE 0350−5658 and WISE 182831.08+265037.8. The sequence of late-T and Y dwarfs becomes bluer at fainter magnitudes, as found in many previous studies (Liu et al. 2012; Dupuy & Kraus 2013; Morley et al. 2014a; Schneider et al. 2015; Leggett et al. 2013, 2015, 2016). That trend has been attributed to the depletion of neutral alkalis into gases and solids (Liu et al. 2012), which would reduce the absorption from pressure-broadened alkali lines at red optical wavelengths (Marley et al. 2002; Burrows et al. 2003). The cloudless models with chemical equilibrium reproduce the Y dwarf sequence in $Y-J$ while the isochrones from the other two suites of models are too red (Liu et al. 2012; Leggett et al. 2013, 2015; Morley et al. 2014a). Tremblin et al. (2015) found that their cloudless models produced similar $Y-J$ colors for equilibrium and non-equilibrium chemistry, both of which matched the data for Y dwarfs. Whereas Y dwarfs have previously exhibited bluer $Y-J$ at fainter magnitudes, our data imply a redder color for WISE 0855−0714. A similar result is found when WISE 0855−0714 is compared to other Y dwarfs in terms of $m_{105}-J$ using F105W photometry from Schneider et al. (2015). As shown in Figure 6, all three sets of models do predict a shift of the Y dwarf sequence back to redder values of $Y-J$ for objects as faint as WISE 0855−0714.

As in the $Y-J$ CMD, a clear extension of the T dwarf sequence is evident among the Y dwarfs in the $J-H$ CMD, except with more discrepant objects in the latter. The blue outliers are WISE J053516.80−750024 and WISE J014656.66+423410.0 and the reddest outlier is WISE 182831.08+265037.8. Previous studies have compared similar $J-H$ CMDs (often with M_J) to model predictions (Morley et al. 2012, 2014a; Leggett et al. 2013, 2015, 2016; Marsh et al. 2013; Beichman et al. 2014), finding that the cloudless and partly cloudy models of Saumon et al. (2012) and Morley et al. (2012, 2014a) tend to produce colors that are too blue (see also Figure 6). Those models agree with the observed colors only if the surface gravity is increased to a value that becomes unphysical for cooler Y dwarfs ($\log g \gtrsim 5$) and the cloud coverage is very large (Morley et al. 2014a). The cloudless non-equilibrium models in Figure 6 are also too blue, although those from Tremblin et al. (2015) are red enough to match the $J-H$ data (Leggett et al. 2016). Previous studies have shown that Y dwarfs start to become redder in $J-H$ at fainter magnitudes (Schneider et al. 2015; Leggett et al. 2015, 2016), and we find that WISE 0855−0714 continues that trend, which agrees with the model predictions (see Figure 6).

3.2.3. *Spectral Energy Distribution*

In Figure 7, we have constructed an SED for WISE 0855−0714 from our photometric measurements in i', F850LP, F105W, F110W, F127M, the CH_4 continuum filter, [3.6], and [4.5]. The other available data in Table 3 are omitted from the SED because they are superseded by our more sensitive photometry in similar bands or they are not deep enough to provide a useful constraint on the models (K_s). As in Figure 1, we include in Figure 7 an example of a model spectrum of a cold brown dwarf (Morley et al. 2014a) to indicate the wavelengths of major spectral features relative to the bands of our photometry.

For each of the three model suites considered in this work and for each of the ages of 1, 3, and 10 Gyr, we have identified the model that has the same value of $M_{4.5}$ as WISE 0855−0714 because this band encompasses most of the flux at <5 μm. For each of those nine models, we then computed the difference between the observed and predicted absolute magnitudes for each of the bands in the SED for WISE 0855−0714. In Figure 7, we plot the resulting differences for the three model suites at 3 Gyr. The temperatures for those best-fit models are 237, 244, an 249 K for cloudless/chemical equilibrium, cloudless/non-equilibrium chemistry, and 50% cloudy, respectively. The other two ages have been omitted because, for a given model suite, most of the magnitude differences for 1, 3, and 10 Gyr span a modest range on

the scale of Figure 7 ($\lesssim$ 0.5 mag). Positive and negative deviations correspond to predicted fluxes that are brighter and fainter than the data, respectively.

For all of the model suites considered, the predicted SEDs exhibit large deviations from the observed SED of WISE 0855−0714. No single model provides a clearly superior match to the data. When the models are selected to match the object at [4.5] as we have done, they are too faint in H and [3.6]. That is a reflection of the fact that the models are too red in $H - [4.5]$ and $[3.6] - [4.5]$, as found in the CMDs. The deviation in H is smallest for the cloudy models, which is also evident from the $H - [4.5]$ CMD in Figure 5. However, the two suites of cloudless models agree better with the SED of WISE 0855−0714 in F850LP through F127M. The cloudy models are too bright by 1.5–2.5 mag in those bands, where the deviation becomes progressively larger at shorter wavelengths.

If one selected a model that matched WISE 0855−0714 in a different band than [4.5], all of the deviations in Figure 7 would shift vertically in the same direction so that the new normalization band exhibited zero deviation. In addition, because the temperature of that model would differ from that derived by fitting to [4.5] and because the near-IR fluxes are more sensitive to temperature than the flux in [4.5], the shifts of the deviations would be larger in the near-IR bands. As with the CMDs, adopting a different band than [4.5] in this analysis does not improve the agreement between the observed SED and the model predictions.

3.3. *Multiplicity Constraints*

Among the images in which WISE 0855−0714 has been detected, those from *HST* offer the highest resolution, and therefore can detect a companion at the smallest separations. The F110W and F127M images have provided the highest S/N for WISE 0855−0714 from among the four filters with which it was observed by *HST*. The S/N in each of those filters is similar to that of the brown dwarf WD 0806-661 B in F110W images from Luhman et al. (2014). Thus, the constraints on the presence of a companion to WISE 0855−0714 are similar to those derived from the images of WD 0806-661 B, which were capable of detecting ∼80% of companions with $\Delta m_{110} \lesssim 0.7$ mag at separations beyond $0\farcs13$ ($\gtrsim 0.3$ AU for WISE 0855−0714).

Because of improvements in the accuracies of parallaxes for Y dwarfs (Dupuy & Kraus 2013; Beichman et al. 2014; Tinney et al. 2014, Section 3.1), the Y dwarf sequence in the $[3.6] - [4.5]$ CMD (Figure 5) is now sufficiently narrow and well-defined that one could attempt to identify unresolved binaries via their elevated positions relative to the sequence. That method is not yet applicable to WISE 0855−0714 since no other Y dwarfs have been found near its absolute magnitude.

4. DISCUSSION

Because of its low temperature, WISE 0855−0714 is very red from near- to mid-IR wavelengths. Its previous detections were limited to one near-IR band (S/N=2.6) and two mid-IR bands. We have presented deep images of WISE 0855−0714 in six optical and near-IR filters, five of which show detections (one is marginal at S/N∼ 3). We also have continued our previous mid-IR imaging of WISE 0855−0714 to refine its parallax.

Using our new photometry and parallax measurement, we have placed WISE 0855−0714 in several CMDs and constructed its SED. For comparison, we have included in the CMDs other known Y dwarfs and the isochrones predicted by three suites of models for the coldest brown dwarfs (Saumon et al. 2012; Morley et al. 2012, 2014a). Previous studies have found that Y dwarfs at fainter magnitudes become bluer in $Y - J$ and begin to become redder in $J - H$ (e.g., Liu et al. 2012; Schneider et al. 2015; Leggett et al. 2016). WISE 0855−0714 is redder than other Y dwarfs in both colors, which confirms the prediction that the near-IR colors of brown dwarfs turn to redder values at temperatures below ∼300–400 K as the Wien tail increasingly affects the colors (Burrows et al. 2003; Saumon et al. 2012; Morley et al. 2014a). No single model is able to reproduce the sequences formed by WISE 0855−0714 and other Y dwarfs in all CMDs. Similarly, the SEDs predicted by all three model suites differ significantly from the SED of WISE 0855−0714. When normalized to the latter in the [4.5] band, the model SEDs are too faint in H and [3.6], which has been found previously for other brown dwarfs (Leggett et al. 2010; Morley et al. 2014a). The deviations at shorter wavelengths exhibit a trend with wavelength, and are particularly large for the cloudy models, which are 1.5–2.5 mag too bright. Because none of the models provide a good match to the SED of WISE 0855−0714, we are unable to determine whether clouds or non-equilibrium chemistry are likely to be present in WISE 0855−0714.

It is not surprising that the predicted and observed SEDs of WISE 0855−0714 differ significantly. The models have not been previously tested at such low temperatures, and several aspects of the models are uncertain, which include the methane opacities, the molecules that are affected by non-equilibrium chemistry, and various aspects regarding the treatment of water clouds (Burrows et al. 2003; Saumon et al. 2012; Morley et al. 2014a). The opacities from the pressure-broadened alkali lines are also uncertain, although those lines should be weak at the temperature of WISE 0855−0714 because of depletion of the alkalis into condensates (Burrows et al. 2003; Morley et al. 2014a). The wavelength dependence of the deviations of the models from the data at < 1.5 μm may provide a clue to their origin (see Figure 7). The current measurement of the SED for WISE 0855−0714 should serve as a valuable test of newer generations of models.

We conclude by discussing the prospects for future observations of WISE 0855−0714. We have presented photometry that covers most of the wavelength range from 0.7–5 μm, so imaging in additional near-IR bands is not essential. Our multiple epochs of photometry in F110W and F127M may show evidence of variability, which could be used to detect clouds and hot spots if measured in greater detail (Morley et al. 2014b). However, it may not be feasible to measure time-series photometry with sufficient accuracy and cadence given that a single *HST* detection with S/N∼10 requires a few hours of observing time. Near-IR spectroscopy of WISE 0855−0714 may be possible with *HST*. Based on our photometry and previous spectroscopy of Y dwarfs (e.g., Cushing et al. 2011;

Schneider et al. 2015), a minimum of 20–30 orbits would be needed to reach S/N$\sim$ 5 in a low-resolution near-IR spectrum of WISE 0855−0714. The *James Webb Space Telescope* will be capable of obtaining near- and mid-IR spectra of it with significantly higher S/N and resolution (Morley et al. 2014a).

We thank Caroline Morley and Didier Saumon for providing their model calculations. We acknowledge support from grants GO-13802 and GO-14157 from the Space Telescope Science Institute and a grant from NASA issued by the Jet Propulsion Laboratory (JPL), California Institute of Technology. The *Spitzer Space Telescope* is operated by JPL/Caltech under a contract with NASA. The NASA/ESA *Hubble Space Telescope* is operated by the Space Telescope Science Institute and the Association of Universities for Research in Astronomy, Inc., under NASA contract NAS 5-26555. Gemini Observatory is operated by AURA under a cooperative agreement with the NSF on behalf of the Gemini partnership: the NSF (United States), the NRC (Canada), CONICYT (Chile), the ARC (Australia), Ministério da Ciência, Tecnologia e Inovação (Brazil) and Ministerio de Ciencia, Tecnología e Innovación Productiva (Argentina). 2MASS is a joint project of the University of Massachusetts and the Infrared Processing and Analysis Center (IPAC) at Caltech, funded by NASA and the NSF. The Center for Exoplanets and Habitable Worlds is supported by the Pennsylvania State University, the Eberly College of Science, and the Pennsylvania Space Grant Consortium.

REFERENCES

Allard, F., Hauschildt, P. H., Baraffe, I., & Chabrier, G. 1996, ApJ, 465, L123
Beamin, J. C., Ivanov, V. D., Bayo, A., et al. 2014, A&A, 570, L8
Beichman, C., Gelino, C. R., Kirkpatrick, J. D., et al. 2013, ApJ, 764, 101
Beichman, C., Gelino, C. R., Kirkpatrick, J. D., et al. 2014, ApJ, 783, 68
Burrows, A., Hubbard, W. B., Lunine, J. I., & Liebert, J. 2001, Reviews of Modern Physics, 719, 765
Burrows, A., Sudarsky, D., & Lunine, J. I. 2003, ApJ, 596, 587
Cushing, M. C., Kirkpatrick, J. D., Gelino, C. R., et al. 2011, ApJ, 743, 50
Cushing, M. C., Kirkpatrick, J. D., Gelino, C. R., et al. 2014, AJ, 147, 113
Dupuy, T. J., & Kraus, A. L. 2013, Science, 341, 1492
Dupuy, T. J., & Liu, M. C. 2012, ApJS, 201, 19
Esplin, T. L., & Luhman, K. L. 2016, AJ, 151, 9
Faherty, J. K., Tinney, C. G., Skemer, A., & Monson, A. J. 2014, ApJ, 793, L16
Fazio, G. G., Hora, J. L., Allen, L. E., et al. 2004, ApJS, 154, 10
Kimble, R. A., MacKenty, J. W., O'Connell, R. W., & Townsend, J. A. 2008, Proc. SPIE, 7010, 43
Kirkpatrick, J. D., Cushing, M. C., Gelino, C. R., et al. 2011, ApJS, 197, 19
Kirkpatrick, J. D., Cushing, M. C., Gelino, C. R., et al. 2013, ApJ, 776, 128
Kirkpatrick, J. D., Gelino, C. R., Cushing, M. C., et al. 2012, ApJ, 753, 156
Kissler-Patig, M., Pirard, J.-F., Casali, M., et al. 2008, A&A, 491, 941
Kopytova, T. G., Crossfield, I. J. M., Deacon, N. R., et al. 2014, ApJ, 797, 3
Leggett, S. K., Burningham, B., Saumon, D., et al. 2010, ApJ, 710, 1627
Leggett, S. K., Morley, C. V., Marley, M. S., et al. 2013, ApJ, 763, 130
Leggett, S. K., Morley, C. V., Marley, M. S., & Saumon, D. 2015, ApJ, 799, 37
Leggett, S. K., Tremblin, P., Saumon, D., et al. 2016, ApJ, in press
Liu, M. C., Deacon, N. R., Magnier, E. A., et al. 2011, ApJ, 740, L32
Liu, M. C., Dupuy, T. J., Bowler, B. P., Leggett, S. K., & Best, W. M. J. 2012, ApJ, 758, 57
Lodieu, N., Béjar, V. J. S., & Rebolo, R. 2013, A&A, 550, L2
Luhman, K. L. 2014, ApJ, 786, L18
Luhman, K. L., Burgasser, A. J., & Bochanski, J. J. 2011, ApJ, 730, L9
Luhman, K. L., Burgasser, A. J., Labbé, I., et al. 2012, ApJ, 744, 135
Luhman, K. L., & Esplin, T. L. 2014, ApJ, 796, 6
Luhman, K. L., Morley, C. V., Burgasser, A. J., Esplin, T. L., & Bochanski, J. J. 2014, ApJ, 794, 16
Mainzer, A., Bauer, J., Cutri, R. M., et al. 2014, ApJ, 792, 30
Marley, M. S., & Robinson, T. D. 2015, ARA&A, 53, 279
Marley, M. S., Saumon, D., Guillot, T., et al. 1996, Science, 272, 1919
Marley, M. S., Seager, S., Saumon, D., et al. 2002, ApJ, 568, 335
Marsh, K. A., Wright, E. L., Kirkpatrick, J. D. et al. 2013, ApJ, 762, 119
Melso, N. D., Kaldon, K. M., & Luhman, K. L. 2015, AJ, 150, 62
Morley, C. V., Fortney, J. J., Marley, M. S., et al. 2012, ApJ, 756, 172
Morley, C. V., Marley, M. S., Fortney, J. J., & Lupu, R. 2014b, ApJ, 789, L14
Morley, C. V., Marley, M. S., Fortney, J. J., et al. 2014a, ApJ, 787, 78
Nakajima, T., Oppenheimer, B. R., Kulkarni, S. R., et al. 1995, Nature, 378, 463
Oppenheimer, B. R., Kulkarni, S. R., Nakajima, T., & Matthews, K. 1995, Science, 270, 1478
Pinfield, D. J., Gromadzki, M., Leggett, S. K., et al. 2014, MNRAS, 444, 1931
Saumon, D., & Marley, M. S. 2008, ApJ, 689, 1327
Saumon, D., Marley, M. S., Abel, M., Frommhold, L., & Freedman, R. S. 2012, ApJ, 750, 74
Schneider, A. C., Cushing, M. C., & Kirkpatrick, J. D., et al. 2015, ApJ, 804, 92
Sirianni, M., Jee, M. J., Benítez, M., et al. 2005, PASP, 117, 836
Skrutskie, M., Cutri, R. M., Stiening, R., et al. 2006, AJ, 131, 1163
Tinney, C. G., Faherty, J. K., Kirkpatrick, J. D., et al. 2012, ApJ, 759, 60
Tinney, C. G., Faherty, J. K., Kirkpatrick, J. D., et al. 2014, ApJ, 796, 39
Tokunaga, A. T., Simons, D. A., & Vacca, W. D. 2002, PASP, 114, 180
Tremblin, P., Amundsen, D. S., Mourier, P., et al. 2015, ApJ, 804, L17
Werner, M. W., Roellig, T. L., Low, F. J., et al. 2004, ApJS, 154, 1
Wright, E. L., Eisenhardt, P. R. M., Mainzer, A. K., et al. 2010, AJ, 140, 1868
Wright, E. L., Mainzer, A., Kirkpatrick, J. D., et al. 2014, AJ, 148, 82

TABLE 1
Observing Log

Telescope/Instrument	Filter	N×τ_{exp} (sec)	Date[a]	Program ID
Spitzer/IRAC	[3.6]	5×23.6	2013 Jun 21	90095
Spitzer/IRAC	[4.5]	5×26.8	2013 Jun 21	90095
Spitzer/IRAC	[4.5]	5×26.8	2014 Jan 20	90095
Spitzer/IRAC	[4.5]	5×26.8	2014 Feb 24	90095
Spitzer/IRAC	[3.6]	9×26.8	2014 Jul 1	10168
Spitzer/IRAC	[4.5]	9×26.8	2014 Jul 1	10168
HST/WFC3	F110W	6×903	2014 Nov 25	13802
VLT/HAWK-I	CH_4 cont	50×100	2014 Dec 1	094.C-0048
VLT/HAWK-I	CH_4 cont	25×100	2015 Jan 9	094.C-0048
VLT/HAWK-I	CH_4 cont	25×100	2015 Jan 15	094.C-0048
VLT/HAWK-I	CH_4 cont	50×100	2015 Jan 17	094.C-0048
VLT/HAWK-I	CH_4 cont	50×100	2015 Jan 19	094.C-0048
VLT/HAWK-I	CH_4 cont	30×100	2015 Jan 20	094.C-0048
Spitzer/IRAC	[3.6]	9×26.8	2015 Jan 29	10168
Spitzer/IRAC	[4.5]	9×26.8	2015 Jan 29	10168
HST/WFC3	F110W	6×903	2015 Mar 3	13802
Spitzer/IRAC	[4.5]	5×26.8	2015 Mar 5	10168
Spitzer/IRAC	[3.6]	405×93.6	2015 Mar 10	11056
Spitzer/IRAC	[4.5]	405×96.8	2015 Mar 9	11056
HST/WFC3	F110W	6×903	2015 Apr 11	13802
Spitzer/IRAC	[4.5]	5×26.8	2015 Jul 6	10168
Spitzer/IRAC	[3.6]	405×93.6	2015 Aug 3	11056
Spitzer/IRAC	[4.5]	405×96.8	2015 Aug 3	11056
Gemini South/GMOS	i'	12×609	2015 Nov 21	GS-2015B-Q-16
Gemini South/GMOS	i'	4×609	2015 Dec 13	GS-2015B-Q-16
Gemini South/GMOS	i'	7×609	2016 Jan 9	GS-2015B-Q-16
Gemini South/GMOS	i'	17×609	2016 Jan 10	GS-2015B-Q-16
HST/WFC3	F105W	6×903	2016 Mar 22	14157
HST/ACS	F850LP	6×810	2016 Mar 23	14157
HST/WFC3	F105W	6×903	2016 Mar 23	14157
HST/ACS	F850LP	6×810	2016 Mar 24	14157
HST/ACS	F850LP	6×810	2016 Mar 24	14157
HST/WFC3	F127M	6×903	2016 Mar 27	14157
HST/WFC3	F105W	6×903	2016 Mar 28	14157
HST/WFC3	F127M	6×903	2016 Mar 28	14157
HST/WFC3	F127M	6×903	2016 Apr 6	14157

[a] For VLT and Gemini, the dates apply to the beginning of the nights of the observations. For *Hubble* and *Spitzer*, the UT dates of the observations are listed.

TABLE 2
Astrometry of WISE J085510.83−071442.5

α (J2000) (°)	σ_α (″)	δ (J2000) (°)	σ_δ (″)	MJD	Source
133.7952573	0.125	−7.2450910	0.135	55320.38	*WISE*
133.7943232	0.133	−7.2450719	0.142	55511.35	*WISE*
133.7881778	0.025	−7.2445255	0.025	56464.51	*Spitzer*
133.7870855	0.025	−7.2444659	0.025	56677.29	*Spitzer*
133.7868470	0.025	−7.2444642	0.025	56712.35	*Spitzer*
133.7858416	0.025	−7.2443262	0.025	56839.71	*Spitzer*
133.7851503	0.025	−7.2443041	0.025	56986.82	*HST*
133.7847553	0.025	−7.2442609	0.025	57051.25	*Spitzer*
133.7843602	0.020	−7.2442366	0.020	57084.82	*HST*
133.7845153	0.025	−7.2442655	0.025	57086.16	*Spitzer*
133.7840688	0.020	−7.2441796	0.020	57123.17	*HST*
133.7835385	0.025	−7.2441445	0.025	57209.43	*Spitzer*
133.7819058	0.020	−7.2440115	0.020	57474.62	*HST*
133.7818923	0.020	−7.2440157	0.020	57475.41	*HST*
133.7818300	0.020	−7.2440063	0.020	57484.38	*HST*

Note. — The *WISE* data are from Wright et al. (2014) after the adjustments described by Luhman & Esplin (2014).

TABLE 3
PHOTOMETRY OF WISE J085510.83−071442.5

Band	Magnitude	Reference
i'	>27.2[a]	1
z'	>24.3[a]	2
m_{850}	$26.85^{+0.31}_{-0.44}$	1
Y	>24.4[a]	3
m_{105}	27.33±0.19	1
m_{110}	26.71±0.19	1
m_{110}	26.47±0.13	1
m_{110}	26.00±0.12	1
m_{127}	24.52±0.12	1
m_{127}	24.49±0.11	1
m_{127}	24.36±0.09	1
J	$25.0^{+0.33}_{-0.53}$	4
CH_4 cont	23.2±0.2	1
H	> 22.7[a]	5
K_s	> 18.6[a]	6
$W1$	17.82±0.33	5
$W2$	14.02±0.05	5
[3.6]	17.44±0.05	1
[3.6]	17.30±0.05	1
[3.6]	17.34±0.02	8
[3.6]	17.28±0.02	8
[4.5]	13.88±0.02	1
[4.5]	13.90±0.02	1
[4.5]	13.92±0.02	1
[4.5]	13.93±0.02	1
[4.5]	13.86±0.02	1
[4.5]	13.82±0.02	1
[4.5]	13.84±0.02	8
[4.5]	13.86±0.02	1
[4.5]	13.80±0.02	8

REFERENCES. — (1) this work; (2) Kopytova et al. (2014); (3) Beamin et al. (2014); (4) Faherty et al. (2014); (5) Wright et al. (2014); (6) VISTA Hemisphere Survey; (7) Luhman (2014); (8) T. Esplin, in preparation.

NOTE. — All data are Vega magnitudes. For bands with multiple measurements, the data are listed in the order of the dates of observations from Table 1 with the exception of the second epoch in [3.6], for which a measurement is not presented because of blending with another star.
[a] S/N<3.

TABLE 4
PROPER MOTION AND PARALLAX OF WISE J085510.83−071442.5

Parameter	Value
π	0.449±0.008″
$\mu_\alpha \cos\delta$	$-8.118 \pm 0.008''$ yr^{-1}
μ_δ	$0.680 \pm 0.007''$ yr^{-1}

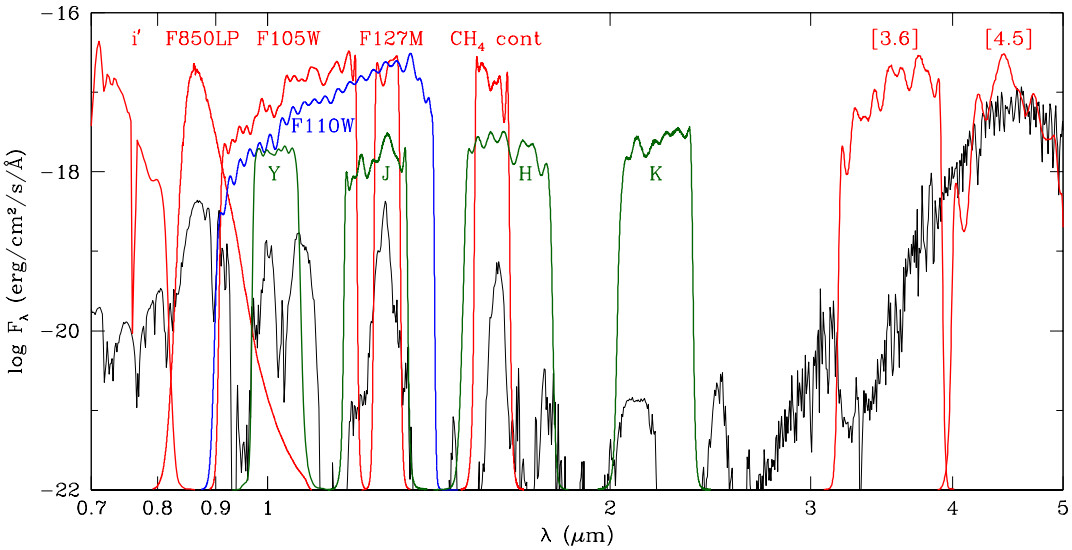

FIG. 1.— Example theoretical spectrum of a cold brown dwarf (250 K at 2 pc, Morley et al. 2014a) compared to the transmission profiles of the bands in which we have obtained images of WISE 0855−0714 (red and blue). For reference, the profiles for Y, J, H, and K (MKO) have been included (green). The profiles are plotted on a linear scale with arbitrary normalizations.

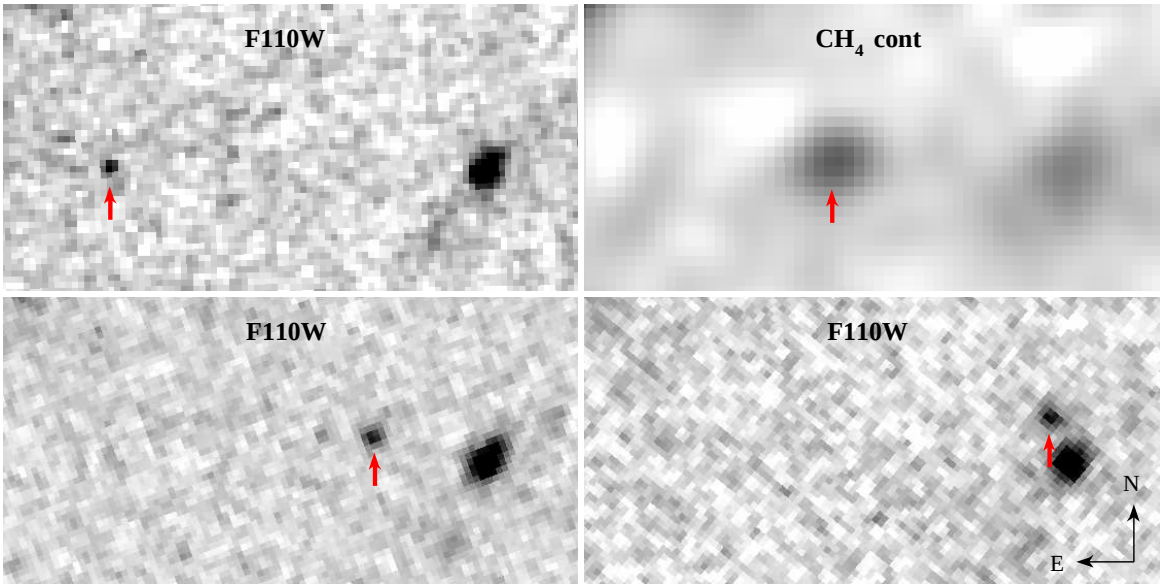

FIG. 2.— Images of WISE 0855−0714 in F110W and a CH_4 continuum filter (see Figure 1). The detections of WISE 0855−0714 are indicated by the arrows. The F110W data were collected on three dates that spanned several months (Table 1). The CH_4 continuum images also were taken across a range of dates. They were registered and combined in a way that compensated for the motion of WISE 0855−0714. The size of each image is $6'' \times 3''$.

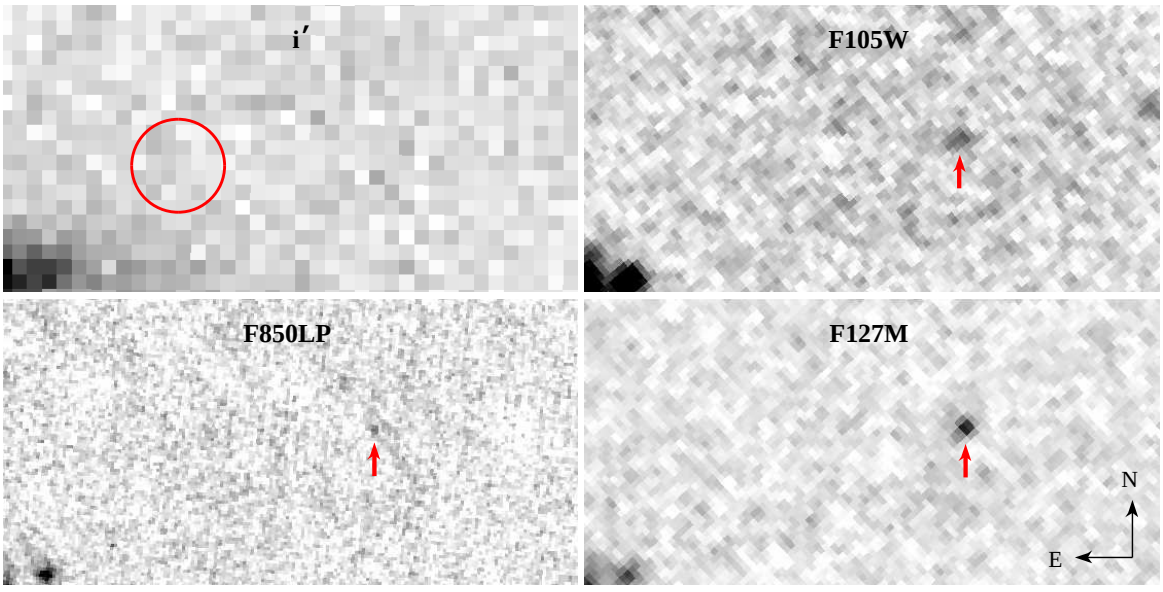

FIG. 3.— Images of WISE 0855−0714 in i', F105W, F850LP, and F127M (see Figure 1). The expected position of WISE 0855−0714 in i' is circled and the detections in the other bands are indicated by the arrows. Each of the F850LP and F105W images is the coaddition of data from six orbits after compensating for the object's motion. The F127M image is from one of the three two-orbit visits in that filter. The field covered by these images is shifted to the west by $\sim 9''$ relative to the field in Figure 2. The size of each image is $6'' \times 3''$.

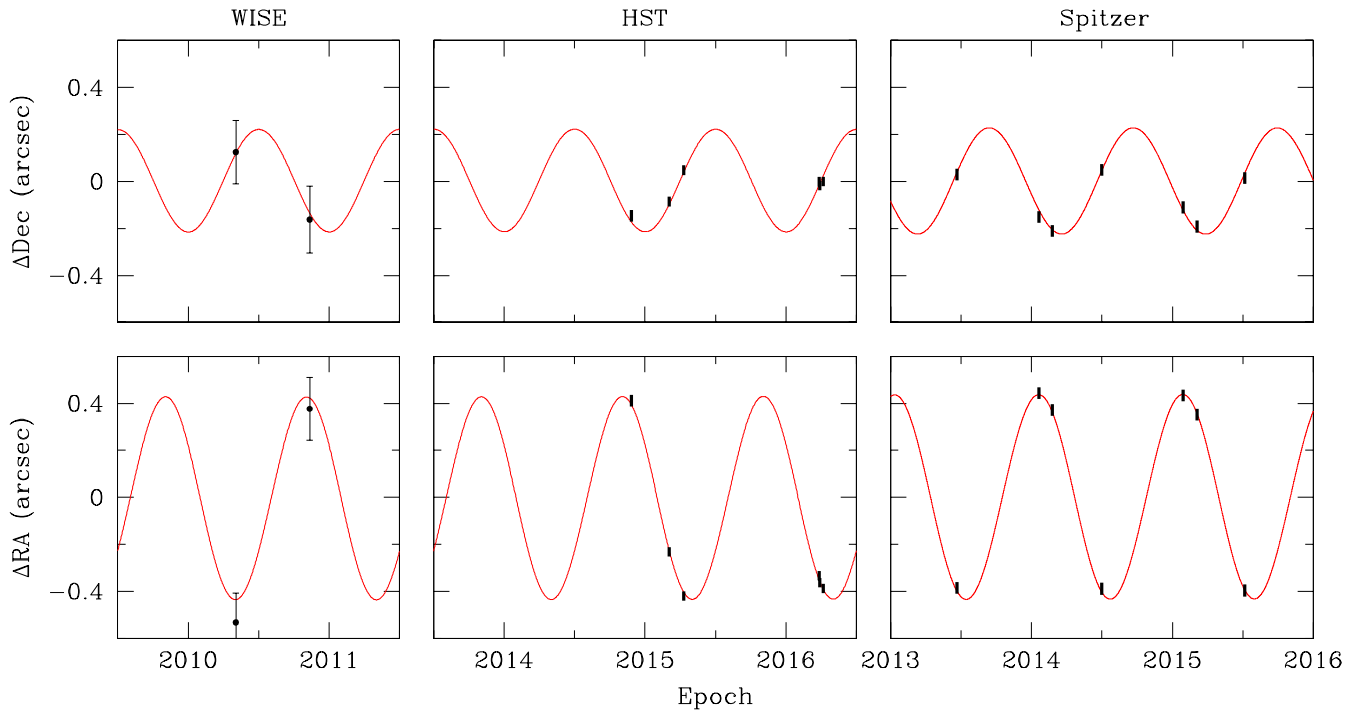

FIG. 4.— Relative astrometry of WISE 0855−0714 (Table 2) compared to the best-fit model of parallactic motion (red curve). The proper motion produced by the fitting has been subtracted.

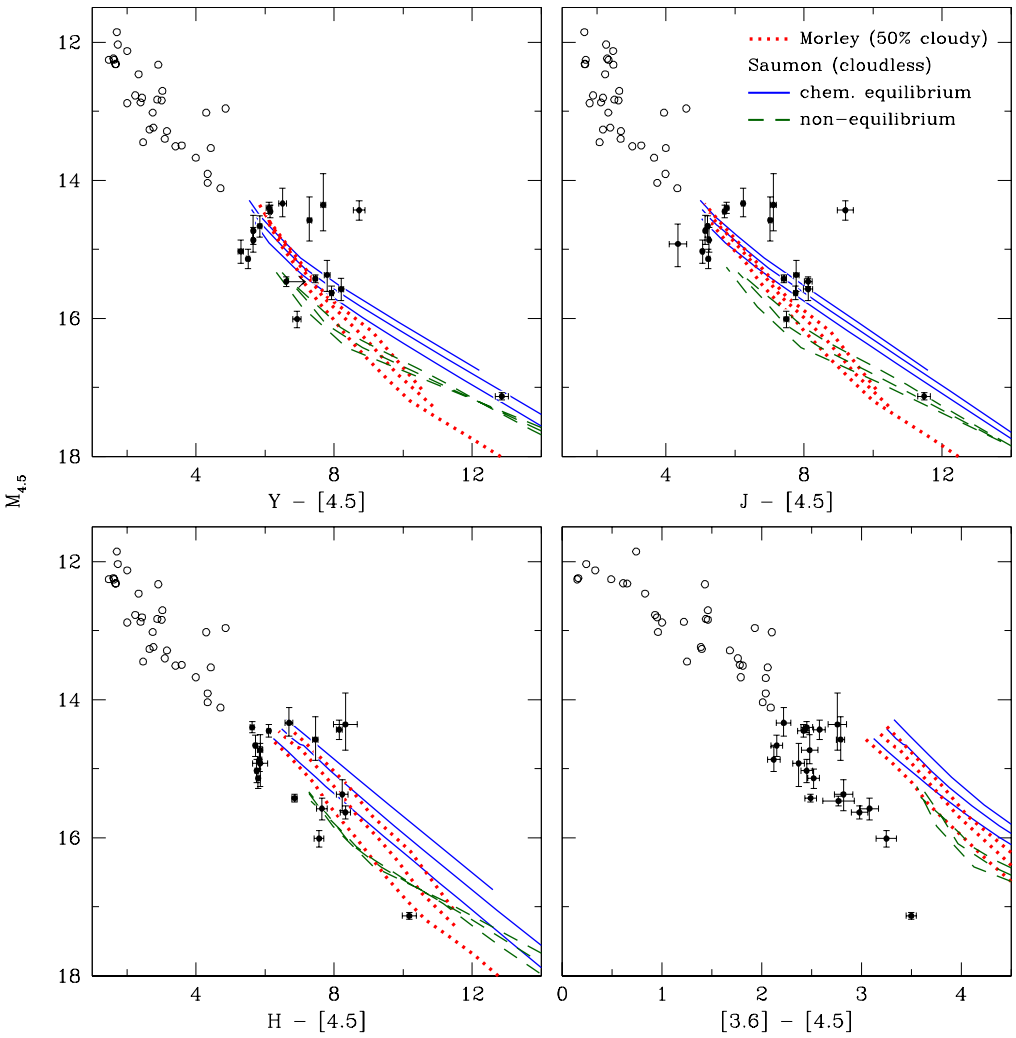

FIG. 5.— Color-magnitude diagrams for WISE 0855−0714 (faintest point) and samples of T dwarfs (open circles, Dupuy & Liu 2012, references therein) and Y dwarfs (filled circles with error bars, Cushing et al. 2011, 2014; Tinney et al. 2012, 2014; Luhman et al. 2012, 2014; Beichman et al. 2013, 2014; Kirkpatrick et al. 2012, 2013; Dupuy & Kraus 2013; Leggett et al. 2013, 2015, 2016; Schneider et al. 2015). These data are compared to the magnitudes and colors predicted by three sets of theoretical models (red solid, blue dotted, and green dashed lines) for ages of 1, 3, and 10 Gyr (Saumon et al. 2012; Morley et al. 2012, 2014a). The Y, J, and H magnitudes for WISE 0855−0714 have been estimated by combining our measurements in F105W, F127M, and the CH_4 continuum filter with the values of $Y - m_{105}$, $J - m_{127}$, and $H - m_{CH4}$ predicted by these models.

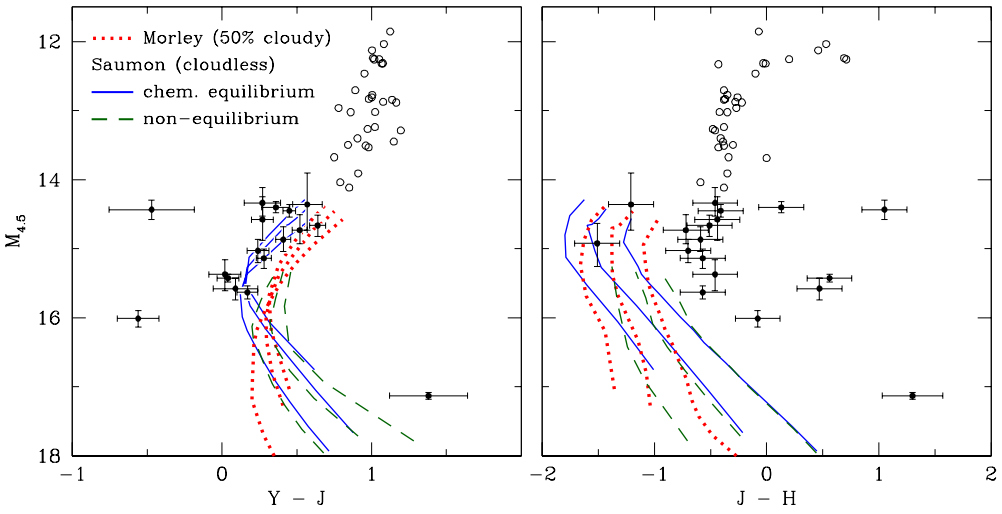

FIG. 6.— Same as Figure 5 for $Y - J$ and $J - H$.

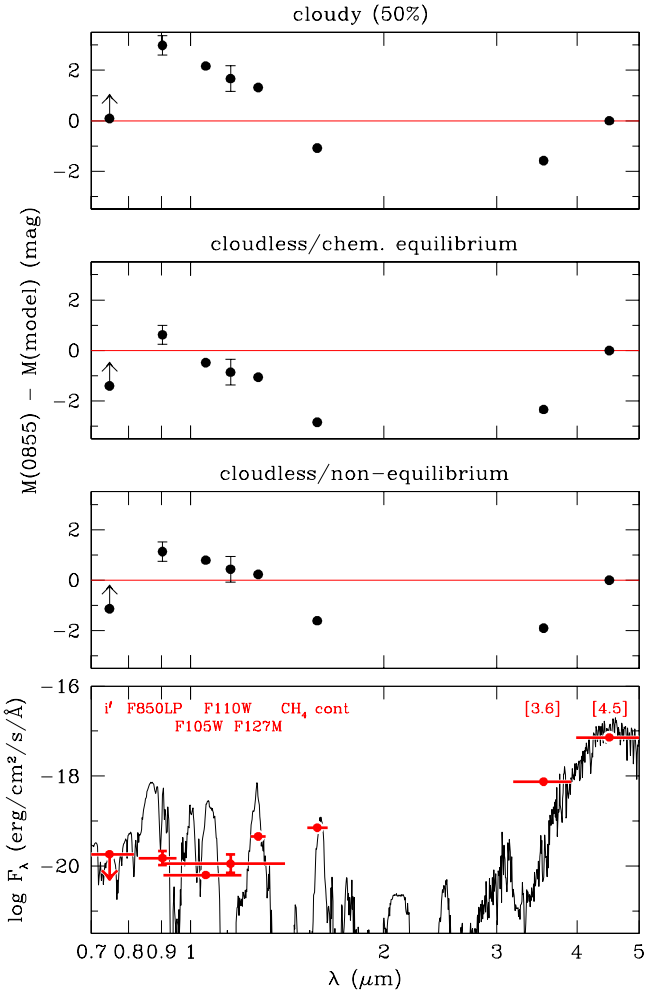

FIG. 7.— Bottom: SED of WISE 0855−0714 (red points) and an example of a theoretical spectrum of a brown dwarf at the distance and $M_{4.5}$ of WISE 0855−0714 (50% cloud coverage, 250 K, Morley et al. 2014a). The horizontal bars on the data points represent the widths of the filters. The vertical bars represent the error in F850LP and the range of the multiple measurements in F110W. The errors in the other bands are smaller than the data points. Top three panels: Differences in absolute magnitudes between WISE 0855−0714 and models that match its $M_{4.5}$ for an age of 3 Gyr (Saumon et al. 2012; Morley et al. 2012, 2014a). A point above/below zero indicates that the predicted flux is brighter/fainter than the observed value.